Clays Clay Miner., Vol. 71, No. 4:448–460, 2023
https://doi.org/10.1007/s42860-023-00249-1

ORIGINAL PAPER

Delaminated and Pit-rich Nano-kaolinites obtained via an Intercalation-etching Method and their Application to Fischer–Tropsch Synthesis

Hongxiao Qu · Tong Liu · Ruijue Hu · Hao Qu · Yichi Zhang · Hui Yang · Haiquan Su · Yue Su

Accepted: 2 August 2023 / Published online: 1 September 2023

Abstract Modified kaolinites possess excellent adsorption properties and, therefore, are regarded widely as potential catalytic components. The use of modified kaolinites as a catalytic component for Fischer–Tropsch synthesis (FTS) has remained unexplored, however. In the current study, delaminated and pit-rich nano-kaolinite was prepared via acid treatment of N-methylformamide (NMF)-intercalated kaolinite (intercalation-etching strategy), and was used as a support to prepare a cobalt-based FTS catalyst (denoted as 15%-Co-HNKln). Compared with other FTS catalysts, the supports for which were raw kaolinite or directly acid-treated kaolinite, the 15%-Co-HNKln showed several advantages such as large specific surface area, dispersed Co particles with small particle size, more new active sites, and significant surface acidity. Given the aforementioned advantages, the 15%-Co-HNKln catalyst demonstrated very good FTS performance. Compared with that of the raw kaolinite-supported FTS catalyst, the CO conversion rate and C_5–C_{12} hydrocarbon selectivity of 15%-Co-HNKln increased by 20% and 15%, respectively.

Keywords Acid treatment · Cobalt-based catalyst · Fischer–Tropsch synthesis · Intercalation · Modified kaolinite

Associate Editor: Runliang Zhu

Supplementary Information The online version contains supplementary material available at https://doi.org/10.1007/s42860-023-00249-1.

H. Qu · T. Liu · R. Hu · H. Qu · Y. Zhang · H. Yang · H. Su
Inner Mongolia Key Laboratory of Chemistry and Physics of Rare Earth Materials, School of Chemistry and Chemical Engineering, Inner Mongolia University, Hohhot 010021, China

Y. Su (✉)
School of Ecology and Environment, Inner Mongolia University, Hohhot 010021, China
e-mail: suyue@imu.edu.cn

Introduction

Kaolinite is among the best known clay minerals and an important industrial material. The chemical formula of kaolinite is $Al_2O_3{\cdot}2SiO_2{\cdot}2H_2O$, and it has a structure of 1:1 dioctahedral layers where each layer consists of a single silica tetrahedral sheet and a single alumina octahedral sheet (Abdullahi & Othman, 2017; Gruner, 1932; Hendricks, 1936). Much research has been devoted to the modification of kaolinite to improve its performance in certain fields (Chen & Lu, 2014; Hai & Asuha, 2015). The application of kaolinite is found in diverse fields, and employing modified kaolinite as a catalytic component is appealing due to its excellent adsorption properties (Li & Dionysiou, 2018, Li & Sun, 2020). Catalytic reactions producing renewable fuels are of interest, among which the Fischer–Tropsch synthesis (FTS) is a hotspot owing

to its ability to convert syngas (CO and H_2) to valuable chemicals or fuels (Fischer & Tropsch, 1926). Exploring the use of kaolinite as a catalytic component for FTS is, thus, a worthwhile venture.

To make kaolinite more suitable for catalytic applications, such as FTS, a proper modification is required. Certain characteristics of raw kaolinite, such as small specific surface area and thick stacking layers, are known to be detrimental to catalytic performance (Qu & Yang, 2023). The most common solution to this problem is to modify the kaolinite via the intercalation-delamination/exfoliation method, which effectively reduces the thickness of stacking layers of kaolinite and leads to increases in the specific surface area and the number of reactive sites. The intercalation-delamination/exfoliation method has been studied widely since the lattice expansion of kaolin minerals treated with potassium acetate, as investigated by Wada (1961). One of the intercalation-delamination/exfoliation agents used commonly is dimethylsulfoxide (DMSO) (Abukhadra & Luqman, 2021; Tian & Ibrahim, 2020; Zuo & Yang, 2018). Nevertheless, for certain catalytic reactions such as FTS, the residual sulfur in the DMSO-intercalated kaolinite will poison the catalyst and, therefore, deactivate the catalytic reaction. Introducing non-sulfur intercalation agents would, therefore, be beneficial to FTS. The dielectric properties of intercalated kaolinites were investigated by Orzechowski and Głowinski (2006) who found that N-methylformamide (NMF) was intercalated almost perfectly, whereas, in the case of potassium acetate, the estimated efficiency was only 81%. Therefore, for the current study, the non-sulfur NMF is an excellent alternative to the DMSO.

Besides delaminating/exfoliating the kaolinite layers, creating pores/pits on the surface of kaolinite is also favorable to catalytic reactions. The surface pores/pits can not only increase the specific surface area but also confine the size of the active component (Lim & Aditya, 2018; Prieto & De Jongh, 2014; Wang & Zhang, 2017). Hierarchical structure kaolinite nanospheres with abundant mesopores were reported by Zhang & Liu (2019). These kaolinite nanospheres had a much greater specific surface area than the raw kaolinite and calcined kaolinite, thus showing excellent adsorption performance with high uptake efficiency to Methylene Blue. An Au/CeO_2 catalyst with a high density of surface pits, which was used for low-temperature CO oxidation was demonstrated by Cai and Guo (2022). The surface pits confined the Au species and made them resistant to sintering. As a result, stabilized Au species were formed on the CeO_2 support, and the Au/CeO_2 catalyst showed high stability (Cai & Guo, 2022). Hence, delaminated/exfoliated kaolinite with surface pores/pits are expected to be more suitable for FTS than raw kaolinite.

To obtain a porous/pitted surface, kaolinite is often treated with acid (Gao & Asuha, 2016; Panda & Singh, 2010); nevertheless the acid-etching process is often inefficient without the delamination/exfoliation of kaolinite. Two problems need to be solved. First, the efficiency of the acid-etching process needs to be improved via the delamination of kaolinite layers. The first objective of the present study, therefore, was to develop a new method that integrates the NMF intercalation with the acid-treatment technique (intercalation-etching) by treating the NMF intercalated kaolinite with nitric acid. The hypothesis was that the delamination and etching process could occur simultaneously, which would improve the etching efficiency. The second objective was to load the delaminated and pit-rich nanokaolinite with Co and then investigate its application as a FTS catalyst. The hypothesis was that Co in the surface pits would be beneficial in improving its FTS performance.

Materials and Methods

Materials

Natural raw kaolinite (Kln) was purchased from Sigma-Aldrich (Burlington, Massachusetts, USA). NMF (analytical reagent, AR) was obtained from Aladdin (Shanghai, China). Nitric acid (AR), cobalt nitrate hexahydrate ($Co(NO_3)_2{\cdot}6H_2O$, AR), and absolute ethanol were purchased from Tianjin Fengchuan Chemical Reagent Co., Ltd (Tianjin, China). All chemicals were used directly without further purification.

Preparation of NMF-Intercalated Kaolinite

10.00 g of kaolinite was dispersed in 100 mL of NMF solution and the mixture was stirred at 80℃ for 24 h. The resulting product was collected by centrifuging

https://doi.org/10.1007/s42860-023-00249-1 Published online by Cambridge University Press

and washed several times with ethanol. Then the solid was dried at 60°C for 12 h to obtain a NMF-kaolinite intercalation complex, which is denoted as NMF-Kln.

Acid Treatment of Kaolinite Samples

5.00 g raw kaolinite was added to a 100 mL flask, and then 50 mL of 2.5 mol/L nitric acid was added. The mixture was stirred magnetically at 50℃ for 24 h. Then the resulting product was centrifuged and dried at 60°C for 24 h. The sample obtained was labeled as HNO_3-Kln. To make a comparison, the NMF-Kln was also treated with nitric acid, which shared the same procedure with the acid treatment of HNO_3-Kln, and the product was denoted as HNO_3-NMF-Kln.

Preparation of FTS Catalysts

The FTS catalysts were prepared by loading Co particles on the kaolinite samples through the wet impregnation method. Typically, 0.89 g of $Co(NO_3)_2{\cdot}6H_2O$ was dissolved in 10.00 mL of deionized water to prepare a salt solution. Subsequently, 1.00 g of Kln was added to the salt solution and stirred at room temperature for 1 h. Then, the mixture was treated with ultrasonic-assisted impregnation for 1 h. The sample obtained was retrieved by centrifugation and dried at 110℃ for 24 h. Subsequently, the sample was crushed to powder and heated from room temperature to 350℃ with the heating rate of 2℃ min^{-1}. The calcination process was maintained for 4 h at 350℃ in air. As a result, the Kln was loaded with Co_3O_4 particles, which was the precursor of a FTS catalyst. Because the nominal loading content of Co particles was 15 wt.%, the precursor was named as 15%-Co_3O_4-Kln. The HNO_3-Kln and HNO_3-NMF-Kln were treated with the same procedure and the precursor FTS catalysts achieved were denoted as 15%-Co_3O_4-HKln and 15%-Co_3O_4-HNKln, respectively.

To convert the precursors into freshly reduced FTS catalysts, the 15%-Co_3O_4-Kln, 15%-Co_3O_4-HKln, and 15%-Co_3O_4-HNKln went through an in situ reduction at 380℃ for 10 h under a H_2 atmosphere. Because the Co_3O_4 on the precursors was reduced to Co(0) after pretreating with H_2, the freshly reduced FTS catalysts were labeled as 15%-Co-Kln, 15%-Co-HKln, and 15%-Co-HNKln, respectively.

Characterization

X-ray diffraction patterns (XRD) were obtained on a Malvern Panalytical (Almelo, Netherlands) X'Pert PRO type diffractometer equipped with target CuKα irradiation (λ = 0.15418 nm) at 40 kV and 40 mA, with a scanning speed and slit width of 0.4°2θ/s and 55 mm, respectively, and without the use of a monochromator. The samples characterized by XRD analysis were crushed into powder form. Fourier-transform infrared (FTIR) spectra were obtained using a Thermo Fisher Scientific (Waltham, Massachusetts, USA) Nicolet 6700 FTIR Spectrometer with a DTGS/KBr detector; the resolution and number of scans were 2 cm^{-1} and 40, respectively. The samples characterized by FTIR analysis were diluted about 200 times with KBr, and then pressed into tablets under 2 MPa of pressure. The morphology of the samples was examined using a Hitachi (Tokyo, Japan) S-4800 scanning electron microscope (SEM) and a FEI Tecnai G^2 F20 field-emission transmission electron microscope (TEM). The samples characterized by SEM and TEM analysis were dispersed in 2 mL of ethanol (1 mg) and treated ultrasonically for 30 min. The elemental analysis of catalyst surface was carried out by using a Bruker (Billerica, Massachusetts, USA) energy-dispersive X-ray spectroscopy (EDS) equipped on the HITACHI S-4800 scanning electron microscope. The chemical composition was analyzed by X-ray fluorescence (XRF, ZSX model) manufactured by Rigaku (Tokyo, Japan). The samples characterized by XRF were diluted about 20 times with boric acid and then pressed into tablets. The thermal mass loss of the sample (0.05 g) was analyzed on a Hitachi (Tokyo, Japan) EXSTAR TG/DTA 7300 Thermogravimetry–Differential Thermal Analyzer under a N_2 flow (15 mL/min) with a heating rate of 5°C/min. The amount of elemental Co in the catalysts was determined by the Thermo Jarrell Ash IRIS Advantage inductively coupled plasma-optical emission spectrometer (ICP-OES) manufactured by the Thermo Fisher Scientific (Waltham, Massachusetts, USA). The samples analyzed by ICP-OES were dispersed into aqua regia before testing. H_2-TPR (temperature programmed reaction) and CO-TPD (temperature-programmed desorption) were obtained using a ChemAutoII 2920 automated chemisorption analyzer from Micromeritics Instrument Corporation (Norcross, Georgia, USA). The samples characterized

https://doi.org/10.1007/s42860-023-00249-1 Published online by Cambridge University Press

by the H_2-TPR and CO-TPD analysis were crushed into powder form and purged at 200°C under an Ar atmosphere for 2 h.

The average thickness of kaolinite samples and the particle size of Co_3O_4 on the precursors of FTS catalysts were calculated by the Scherrer equation (Scherrer, 1918):

$$L = K \cdot \lambda/\beta \cdot \cos\theta$$

where L represents the crystallite size, K is a dimensionless shape factor, λ represents the X-ray wavelength, β represents the full width at half maximum of peaks, and θ is the Bragg angle.

The intercalation ratio of the NMF-kaolinite intercalation complex (NMF-Kln) was calculated by the intensity of XRD reflections (Wiewióra, 1969):

$$\text{Intercalation Ratio} = [I_{(001)\text{complex}}/(I_{(001)\text{complex}} + I_{(001)\text{kaolinite}})] \times 100\%$$

where $I_{(001)\text{complex}}$ represents the basal peak intensity of NMF-kaolinite intercalation complex, and $I_{(001)\text{kaolinite}}$ represents the basal peak intensity of unexpanded kaolinite component in the complex.

Catalytic Evaluation

0.8 g of each freshly reduced FTS catalyst was used for the evaluation. The catalytic performance was evaluated under reaction conditions of $H_2/CO = 2:1$, $T = 220$℃, and $P = 2.0$ MPa. The composition of off-gas was detected by an online gas chromatography (GC) system (Shimadzu GC-2014C, Japan).

The CO conversion rate of the freshly reduced FTS catalysts was calculated according to mass balance:

$$\text{CO conversion } (\%) = \frac{M_{\text{CO(inlet)}} - M_{\text{CO(off-gas)}}}{M_{\text{CO(inlet)}}} \times 100\%$$

The product selectivity of the freshly reduced FTS catalysts was calculated using the following equation:

$$S_i\ (\%) = \frac{C_i}{\sum C_i} \times 100\%$$

where $M_{\text{CO (inlet)}}$ and $M_{\text{CO (off-gas)}}$ represent moles of CO at the inlet and outlet, respectively. C_i represents the moles of C of the product i.

Results and Discussion

Characterization of Kaolinite Samples

The powder XRD was conducted to identify the crystalline structure of the Kln, HNO_3-Kln, NMF-Kln, and HNO_3-NMF-Kln (Fig. 1). In the case of Kln, the reflection at 12.39°2θ corresponded to the (001) plane of kaolinites, which revealed the stacking degree of layers in the c-axis direction (Zuo and Yang, 2018). The narrow reflection of the (001) plane of Kln indicated a high stacking degree of kaolinite layers. As for HNO_3-Kln, nearly all of the reflections from Kln were retained after the acid-treatment process, and

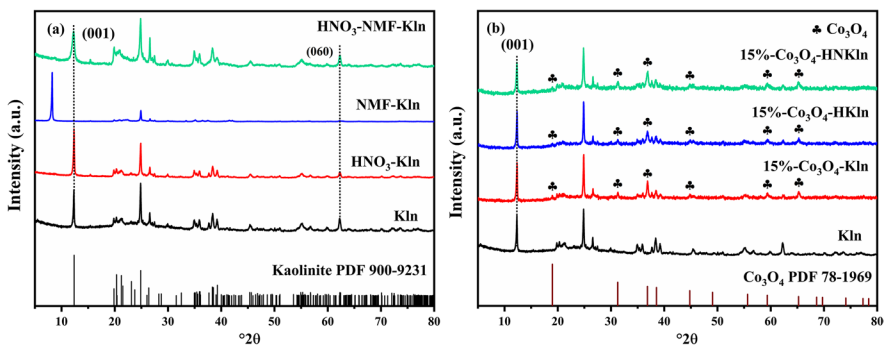

Fig. 1 XRD patterns of **a** kaolinite samples treated by different approaches and **b** 15%-Co_3O_4-Kln, 15%-Co_3O_4-HKln, and 15%-Co_3O_4-HNKln catalyst precursors

https://doi.org/10.1007/s42860-023-00249-1 Published online by Cambridge University Press

moreover, the narrow (001) reflection of HNO_3-Kln indicated that the stacking degree of layers was hardly affected by the direct acid-treating process. After the intercalation of NMF, the reflection of the (001) plane of NMF-Kln shifted to a lower angle (8.23°2θ), which indicated an expansion of the interlayer space, implying that the NMF had been intercalated successfully into the interlayer space of kaolinites (Sugahara & Kato, 1990). According to the formula described in the materials and methods section, the intercalation ratio of NMF was 98%. After treating NMF-Kln with HNO_3 (sample HNO_3-NMF-Kln), the (001) reflection shifted to a higher angle of 12.39°2θ, which was due to the elimination of NMF and the subsequent shrinkage of interlayer space. The FWHM of the (001) reflection of HNO_3-NMF-Kln was obviously larger than that of Kln (0.53 vs 0.18); this was due to the delamination of kaolinites caused by the break-up of hydrogen bonds between the kaolinite layers. According to the Scherrer equation, the average thickness of HNO_3-NMF-Kln was calculated as 14 nm. In addition, all of the kaolinite samples exhibited the reflection located at 62.26°2θ, which was attributed to the (060) plane of kaolinite, reflecting the character of a dioctahedral clay mineral (Letaief & Detellier, 2011). Clearly, the typical dioctahedral structure was preserved in both direct acid-treatment and intercalation-etching process.

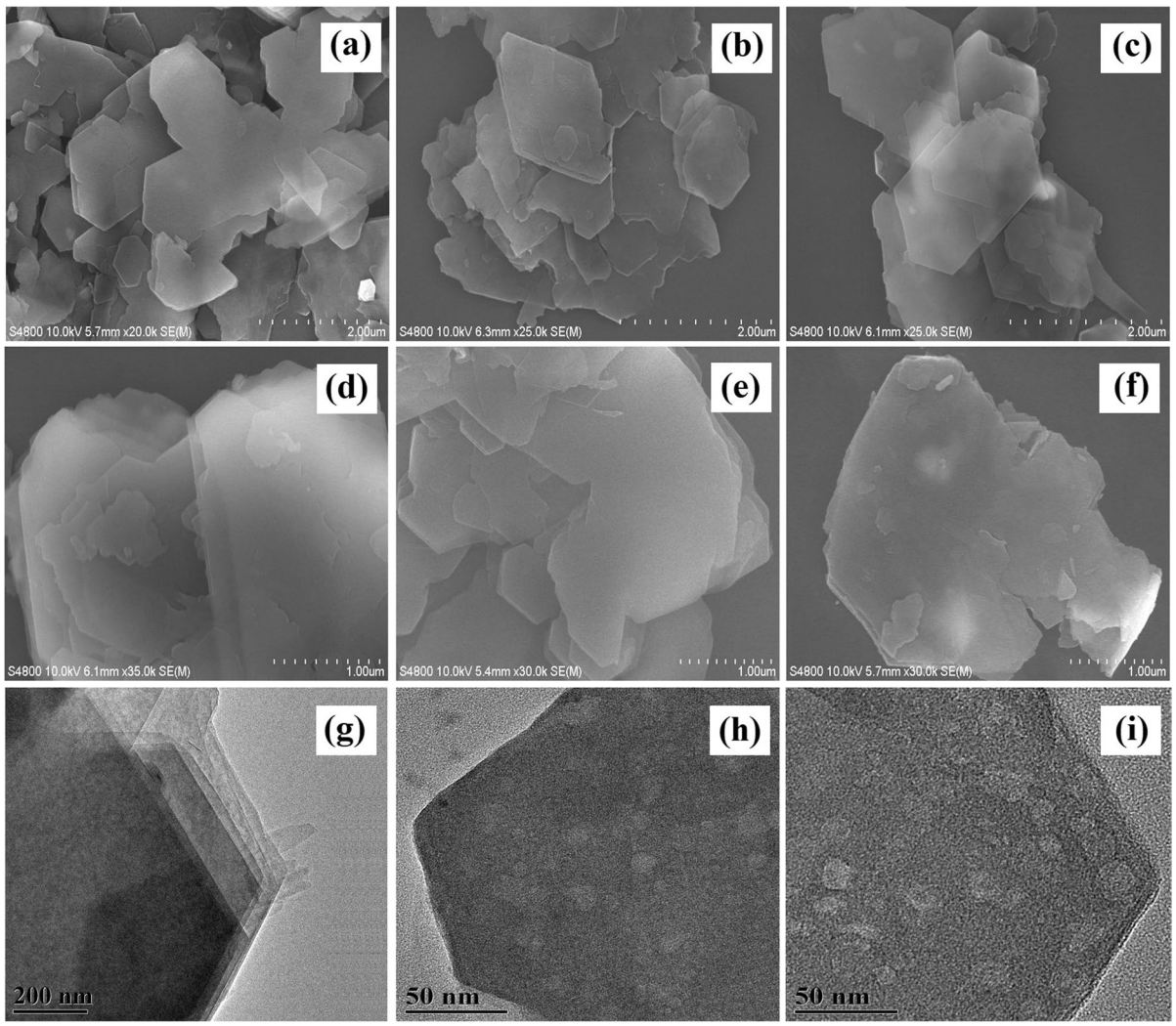

Fig. 2 **a,d** SEM and **g** TEM images of Kln; **b**,**e** SEM, and **h** TEM images of HNO_3-Kln; **c**,**f**, and **i** TEM images of HNO_3-NMF-Kln

https://doi.org/10.1007/s42860-023-00249-1 Published online by Cambridge University Press

The morphology of the kaolinite samples was characterized by SEM and TEM (Fig. 2). The sample Kln (Fig. 2a, d) presented a well-ordered pseudohexagonal lamellar structure with thick stacking layers. After the direct acid-treatment process, the HNO_3-Kln exhibited negligible delamination (Fig. 2b and 2e).The stacking layers of HNO_3-Kln were still thick, with relatively small lamellae due to the etching process. After the intercalation of NMF, the morphology of the sample NMF-Kln exhibited few changes compared with that of Kln (as shown in Supplementary Information Fig. S1). For HNO_3-NMF-Kln, an obvious delamination was observed. As shown in Figs S2 and 2f, the thickness of stacking layers of HNO_3-NMF-Kln was reduced significantly compared with that of Kln, which was consistent with the XRD result. Meanwhile, Fig. 2c shows that the edges of kaolinite nanolayers in HNO_3-NMF-Kln were partially curled and slightly damaged, which was due to the break-up of hydrogen bonds and leaching of the surface during the acid-treatment process. Importantly, the TEM images demonstrated that the surface of HNO_3-Kln (Fig. 2h) and HNO_3-NMF-Kln (Fig. 2i) had many small pits (light spots in the figures) while Kln did not (Fig. 2g). The diameter of these surface pits ranged from ~3 to 17 nm for both samples. The formation of surface pits was due to the removal of Al from Al-O(OH) in kaolinites by H^+ during acid treatment (Hu & Yang, 2013).

To determine the functional groups in the kaolinite samples, FTIR spectra were collected (Fig. 3). In the raw kaolinites, the band at 3620 cm^{-1} belonged to the OH-stretching modes of inner hydroxyl groups, while the bands at 3695 and 3669 cm^{-1} were attributed to inner-surface hydroxyl groups (Zhu & Yan, 2016). Meanwhile, the bands at 1101, 1033, and 1009 cm^{-1} were assigned to the stretching vibration mode of Si–O bonds. After HNO_3 treatment, the FTIR spectrum of HNO_3-Kln was similar to that of Kln, with no new bands and with all original bands still present. Nevertheless, the relative intensity of the bands in 3620–3695 cm^{-1} was weakened for HNO_3-Kln, implying that both types of the hydroxyl groups were reduced due to the removal of Al from Al–O(OH). After NMF intercalation, the band at 3695 cm^{-1} in Kln shifted to 3678 cm^{-1} in NMF-Kln, which was due to the formation of new hydrogen bonds during NMF intercalation (Komori & Kuroda, 1998), proving that NMF was intercalated successfully into the interlayers of kaolinites. Meanwhile, in NMF-Kln, the bands at 2908 and 1350 cm^{-1} belonged to the symmetric stretching and bending vibrations of CH_3, respectively (Tunney & Detellier, 1997), the bands at 3419 and 1529 cm^{-1} were attributed to the stretching and bending vibrations of N–H, respectively, while the band at 1682 cm^{-1} was assigned to the stretching vibration of C=O (Kelleher & O'Dwyer, 2002a, 2002b). All of the bands mentioned above proved further the successful intercalation of NMF into the interlayers of kaolinites. As for HNO_3-NMF-Kln, a weak NMF band at 1684 cm^{-1} was noted in the FTIR spectrum, and the band associated with the new hydrogen bond (3678 cm^{-1}) in NMF-Kln shifted to 3695 cm^{-1} in HNO_3-NMF-Kln, which indicated the breaking of the new hydrogen bond formed during NMF intercalation. The FTIR data of HNO_3-NMF-Kln above demonstrated that most of the NMF was eliminated after HNO_3 treatment. More importantly, the peak area ratio of Si–O bonds (1009 to 1101 cm^{-1}) to inner and inner-surface hydroxyl groups (3620 to 3695 cm^{-1}) of HNO_3-NMF-Kln was greater than that of HNO_3-Kln (4.5 VS 4.2), which indicated that more Al_2O_3 was leached for HNO_3-NMF-Kln due to a more efficient etching process.

The three kaolinite samples were analyzed by XRF (Table 1). The concentration of metal elements is given in the form of oxides. Clearly, the raw kaolinite (Kln) was composed mainly of SiO_2 and Al_2O_3, with small amounts of other metal oxides presented as impurities. After direct acid treatment of raw kaolinite, the chemical composition of HNO_3-Kln was changed slightly, which was due to an insufficient etching process. By contrast, the HNO_3-NMF-Kln showed obvious change in its chemical composition, with SiO_2 increased to 70.10% while Al_2O_3 decreased to 26.14%, which indicated that Al_2O_3 was leached efficiently and selectively during the etching of NMF-Kln. Evidently, the expanded interlayer space of NMF-Kln enabled a more efficient leaching of the internal aluminum atoms due to more nitric acid being able to enter the interlayer space of kaolinite, leading to the sharp decrease in the amount of Al_2O_3 in HNO_3-NMF-Kln. The XRF result was consistent with the TEM and FTIR analysis.

The thermal mass loss of the kaolinite samples was presented as TG and DTG curves (Fig. 4). As can be seen, the Kln, HNO_3-Kln, and HNO_3-NMF-Kln

https://doi.org/10.1007/s42860-023-00249-1 Published online by Cambridge University Press

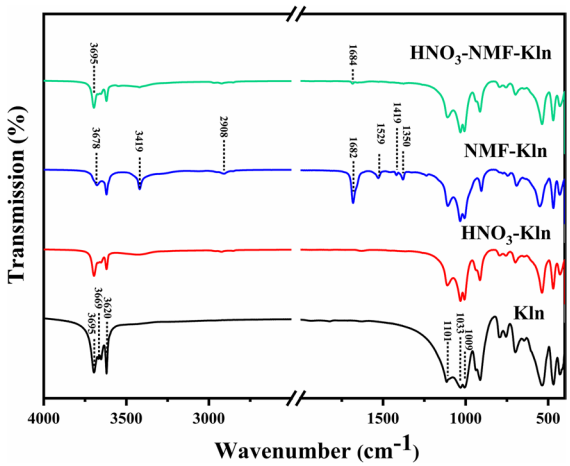

Fig. 3 FTIR spectra of various kaolinite samples

exhibited a mass loss at 500, 494, and 487℃, respectively, all of which were attributed to the dehydroxylation of kaolinite (Horváth & Cseh, 2003). Note that the HNO_3-NMF-Kln not only showed the lowest dehydroxylation temperature among the three samples, but also exhibited a continuous mass loss from 50 to 600℃. The reason for this phenomenon was that more hydroxyl groups in kaolinite were exposed on the surface for HNO_3-NMF-Kln due to the delamination of the layers, thus less energy was required for the dehydroxylation process because these exposed hydroxyl groups could not form hydrogen bonds between the adjacent layers. As for NMF-Kln, two mass-loss peaks could be observed from the TG and DTG curves. The first mass loss at 135°C was attributed to the decomposition of NMF between the kaolinite layers (Adams, 1978; Li & Komarneni, 2017), while the second mass loss, which appeared at 504°C, was assigned to the dehydroxylation of kaolinites, and this temperature was greater than for the other samples. The reason for this increased dehydroxylation temperature was the breaking of new hydrogen bonds formed during NMF intercalation, where more energy was required (Kelleher & O'Dwyer, 2002b; Li & Komarneni, 2017). The results above demonstrated further the successful intercalation and removal of NMF, as well as the delamination of kaolinite layers.

Table 1 Chemical composition (wt.%) of the kaolinite samples analyzed by XRF

Samples Chemical Composition	Kln	HNO_3-Kln	HNO_3-NMF-Kln
SiO_2	57.11	60.85	70.10
Al_2O_3	38.80	35.52	26.14
Fe_2O_3	0.58	0.60	0.27
TiO_2	0.59	0.80	0.84
Na_2O	0.63	0.13	0.02
K_2O	2.16	2.02	2.54
CaO	0.13	0.08	0.09

To investigate the specific surface area and textural structure of the kaolinite samples, BET analysis was conducted. As the N_2-adsorption/desorption isotherms show (Fig. 5), all of the kaolinite samples exhibited a type II isotherm, which represents a nonporous or macroporous solid. In the present cases, all of the samples were macroporous, and the majority of the pores were generated by the accumulation of delaminated kaolinite layers. In addition, HNO_3-NMF-Kln had the largest adsorption volume among all the kaolinite samples, while Kln had the lowest. Interestingly, the absorption volume of NMF-Kln was close to that of HNO_3-NMF-Kln, which was probably due to the expansion of interlayer space caused by the NMF intercalation.

The specific surface area and pore volume of Kln, HNO_3-Kln, NMF-Kln, and HNO_3-NMF-Kln are listed in Table 2. Compared with Kln, the HNO_3-Kln, NMF-Kln, and HNO_3-NMF-Kln exhibited increased specific surface area and pore volume. Note that the HNO_3-NMF-Kln possessed the largest specific surface area and pore volume. A significant increase in specific surface area for HNO_3-NMF-Kln was due to the delamination of kaolinite layers and generation of surface pits, and the delamination process was critical. The increased pore volume for HNO_3-NMF-Kln was due to the generation of more accumulation pores formed by the accumulation of delaminated kaolinite layers. According to the BET analysis, the HNO_3-NMF-Kln would be expected to be the most efficient catalyst support among all the kaolinite samples.

Characterization of the Precursors of FTS Catalysts

After Kln, HNO_3-Kln, and HNO_3-NMF-Kln were loaded with cobalt nitrate hexahydrate and then calcined, the precursors of FTS catalysts were obtained,

https://doi.org/10.1007/s42860-023-00249-1 Published online by Cambridge University Press

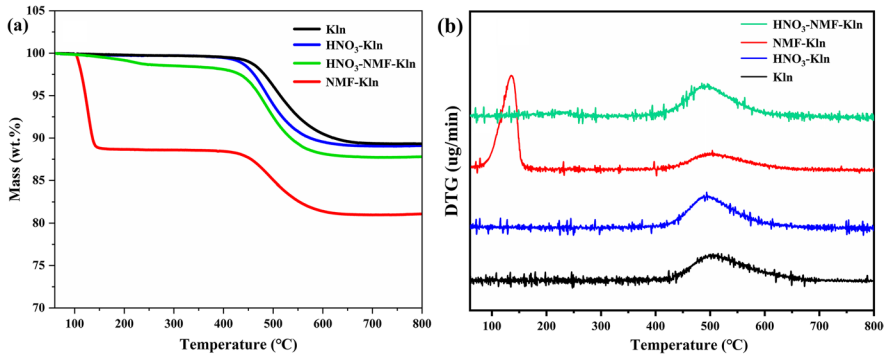

Fig. 4 **a** TG and **b** DTG curves of Kln, HNO_3-Kln, NMF-Kln, and HNO_3-NMF-Kln

which were denoted as 15%-Co_3O_4-Kln, 15%-Co_3O_4-HKln, and 15%-Co_3O_4-HNKln, respectively. Powder XRD was conducted to analyze the crystalline structure of the three precursors (Fig. 1b). Obviously, all of the reflections of raw kaolinites were preserved in the precursors, which indicated that the structure of kaolinite was not destroyed. Meanwhile, new reflections at 18.99°2θ (111), 38.54°2θ (222), and 65.23°2θ (440) appeared in all precursors, which were assigned to Co_3O_4 (PDF: 01–078-1969). According to the Scherrer equation, the average size of Co_3O_4 particles of 15%-Co_3O_4-HKln and 15%-Co_3O_4-HNKln was ~24 and 23 nm, respectively, which was obviously smaller than that of 15%-Co_3O_4-Kln (33 nm). The reason for the reduced Co_3O_4 particle size was probably due to the surface pits of 15%-Co_3O_4-HKln and 15%-Co_3O_4-HNKln. When Co_3O_4 particles were embedded in these pits, the growth of particles was restricted.

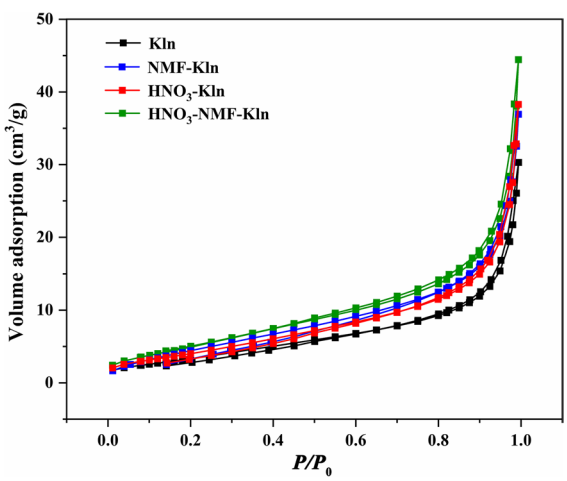

Fig. 5 N_2-adsorption/desorption isotherms of Kln, HNO_3-Kln, NMF-Kln, and HNO_3-NMF-Kln

The morphology and structure of the 15%-Co_3O_4-Kln, 15%-Co_3O_4-HKln, and 15%-Co_3O_4-HNKln precursors were demonstrated in the SEM, TEM, and HRTEM images (Fig. 6). As shown in Fig. 6a–c, the surfaces of the three precursors were covered with small particles which were assigned to Co_3O_4 due to the interplanar distances of these small particles being 0.286 and 0.245 nm (as shown in Fig. 6f), corresponding to the (022) and (311) lattice planes of Co_3O_4, respectively. Besides, the Co_3O_4 particles showed obvious aggregation for 15%-Co_3O_4-Kln, while for 15%-Co_3O_4-HKln and 15%-Co_3O_4-HNKln the Co_3O_4 particles were relatively dispersed, especially for 15%-Co_3O_4-HNKln. The reason 15%-Co_3O_4-HNKln demonstrated the greatest dispersion of Co_3O_4 particles was that it had the largest specific surface area. The TEM images demonstrated that the Co_3O_4 particles of 15%-Co_3O_4-HKln (Fig. 6d) and 15%-Co_3O_4-HNKln (Fig. 6e) were quite uneven in size. The significantly smaller Co_3O_4 particles were probably embedded in the surface pits, while the obviously larger ones

Table 2 Specific surface area and pore volume of Kln, HNO_3-Kln, and HNO_3-NMF-Kln

	Specific surface area (m^2/g)	Pore volume (m^3/g)
Kln	9.75	0.04
HNO_3-Kln	38.43	0.07
NMF-Kln	41.25	0.08
HNO_3-NMF-Kln	47.53	0.10

https://doi.org/10.1007/s42860-023-00249-1 Published online by Cambridge University Press

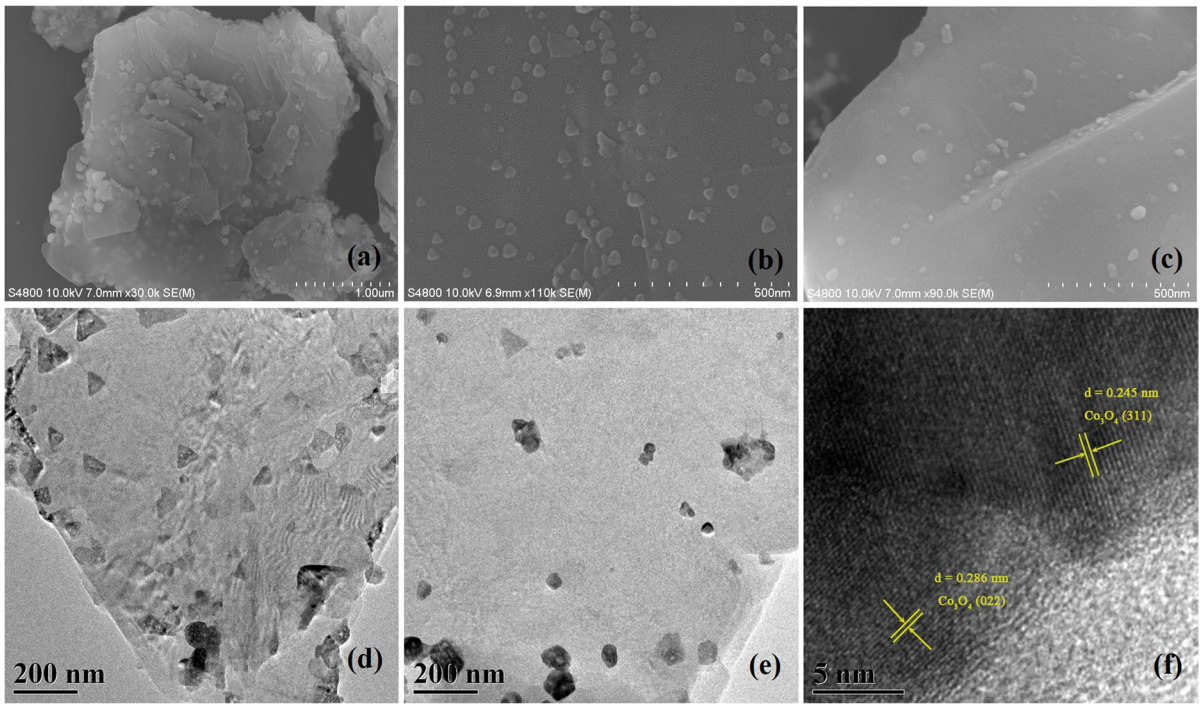

Fig. 6 SEM images (at various magnifications) of **a** 15%-Co_3O_4-Kln, **b** 15%-Co_3O_4-HKln, and **c** 15%-Co_3O_4-HNKln; TEM images of **d** 15%-Co_3O_4-HKln, **e** 15%-Co_3O_4-HNKln, and **f** HRTEM image of 15%-Co_3O_4-HNKln

were simply dispersed on the surface. The embedding strategy has an advantage in controlling the size of metal particles and preventing the migration of metal, thus the small Co_3O_4 particles embedded in the surface pits are very likely to improve the FTS performance. Based on the discussion above, the 15%-Co_3O_4-Kln is expected to be an inferior precursor to 15%-Co_3O_4-HKln and 15%-Co_3O_4-HNKln. Furthermore, due to the delaminated kaolinite layers, the thickness of 15%-Co_3O_4-HNKln was less than that of 15%-Co_3O_4-Kln (as shown in Fig. S3), which was consistent with the thickness of Kln and HNO_3-NMF-Kln support.

EDS mapping was conducted for the three precursors (Fig. S4). The actual distributions of elemental Co revealed that the Co_3O_4 particles of 15%-Co_3O_4-Kln showed obvious aggregation, while 15%-Co_3O_4-HNKln had the most dispersed particles. This result was consistent with the SEM analysis. Meanwhile, as shown in the EDS analysis, the three precursors exhibited similar peak values of Co, which demonstrated similar Co_3O_4 loading amounts among the three precursors.

To determine further the amount of Co in the three precursors of FTS catalysts, ICP-OES was conducted. The loading amounts of Co of 15%-Co_3O_4-Kln, 15%-Co_3O_4-HKln, and 15%-Co_3O_4-HNKln were 16.5, 15.9, and 15.7 wt.%, respectively (Table 3). The similar loading amounts of the three precursors indicated that the loading process was scarcely affected by either direct acid treatment or by the intercalation-etching strategy.

H_2-TPR profiles for all precursors are shown in Fig. 7a. For sample 15%-Co_3O_4-Kln, two peaks centered at 280 and 315°C were observed, which corresponded to the reduction of Co^{3+} to Co^{2+} and Co^{2+} to Co^0, respectively (Irandoust & Haghtalab, 2017).

Table 3 Loading of Co in the catalyst precursors analyzed by ICP-OES

Catalysts	15%-Co_3O_4-Kln	15%-Co_3O_4-HKln	15%-Co_3O_4-HNKln
Co loading (wt.%)	16.5	15.9	15.7

https://doi.org/10.1007/s42860-023-00249-1 Published online by Cambridge University Press

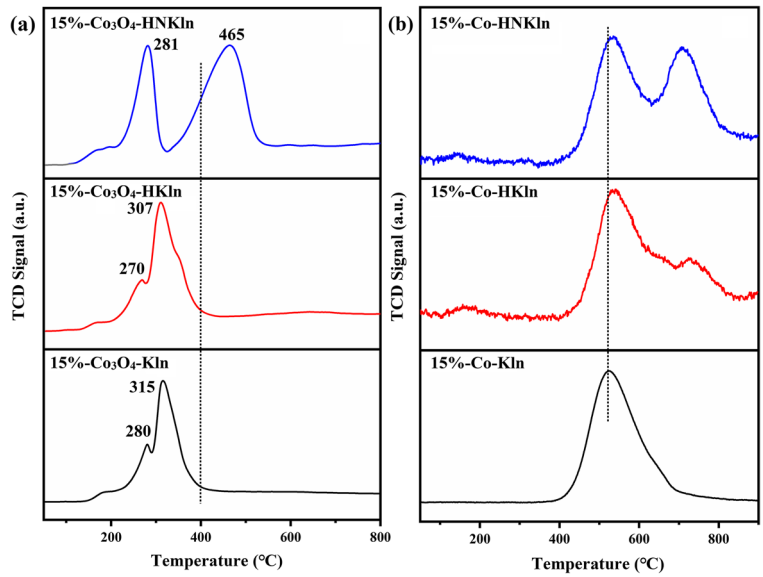

Fig. 7 **a** H_2-TPR of the 15%-Co_3O_4-Kln, 15%-Co_3O_4-HKln, and 15%-Co_3O_4-HNKln precursors and **b** CO-TPD spectra of 15%-Co-Kln, 15%-Co-HKln, and 15%-Co-HNKln catalysts

As for 15%-Co_3O_4-HKln, the reduction temperatures of Co^{3+} to Co^{2+} and Co^{2+} to Co^0 appeared at 270 and 307°C, respectively. A small peak appeared at the right shoulder of the 307°C peak, which was assigned to the reduction of the small CoO particles embedded in the surface pits. As is well known, smaller particles have greater interactions with the support than larger ones, thus a higher temperature was required to reduce the CoO particles (Akbarzadeh & Johan, 2018). For 15%-Co_3O_4-HNKln, the Co^{2+} to Co^0 reduction peak shifted to a much higher temperature of 465℃, which indicated that the interaction between CoO particles and support was much stronger in this sample. In other words, the size of CoO was much smaller for 15%-Co_3O_4-HNKln because this sample had a larger specific surface area and more surface pits, which was beneficial to the dispersion and confinement of CoO particles.

After the three precursors were converted to freshly reduced FTS catalysts (15%-Co-Kln, 15%-Co-HKln, and 15%-Co-HNKln), CO-TPD was conducted to characterize the adsorption and desorption of CO on the surface of the catalysts (Fig. 7b). Through this characterization, the active sites on the surface of the FTS catalysts can be investigated. As shown in the CO-TPD pattern, only one CO desorption peak centered at 522℃ was observed in 15%-Co-Kln, while two major peaks were observed for both 15%-Co-HKln and 15%-Co-HNKln. The desorption peak which appeared at ~ 520℃ in all of the samples belonged to the active sites of normally dispersed Co particles, while the new desorption peak which appeared at ~730℃ in 15%-Co-HKln and 15%-Co-HNKln was assigned to the new active sites of highly dispersed Co particles with small particle size embedded in surface pits. Note that the peak area associated with the new active sites was much larger for 15%-Co-HNKln, which indicated that this sample possessed the largest number of new active sites (or surface pits), implying that 15%-Co-HNKln went through the most efficient acid-etching process. Moreover, rich surface pits were beneficial to the generation of small particles and thus it was reasonable that 15%-Co-HNKln exhibited the greatest CoO reduction temperature as shown in the TPR.

Catalytic Performance

The catalytic performance of freshly reduced FTS catalysts was evaluated under the reaction conditions

https://doi.org/10.1007/s42860-023-00249-1 Published online by Cambridge University Press

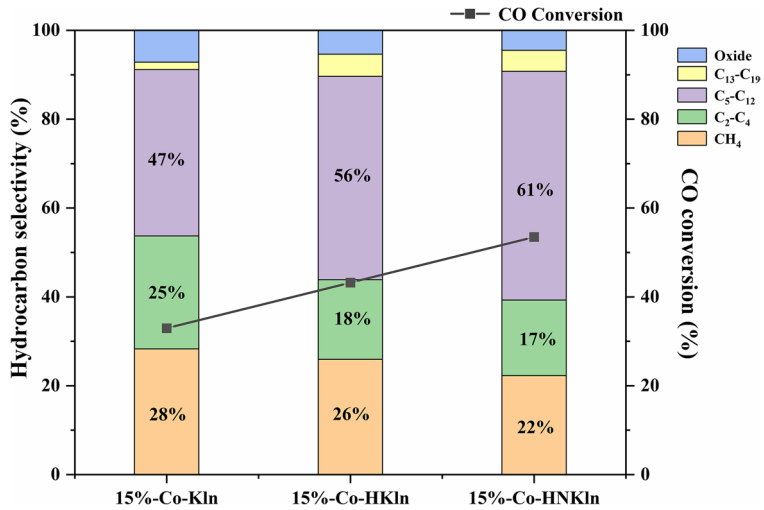

Fig. 8 CO conversion rate and product selectivity of 15%-Co-Kln, 15%-Co-HKln, and 15%-Co-HNKln catalysts

of H_2/CO = 2:1, T = 220℃, and P = 2.0 MPa (Fig. 8, Table 4). Clearly, the CO conversion rate and C_5–C_{12} hydrocarbon selectivity of 15%-Co-HKln and 15%-Co-HNKln were significantly greater than those of 15%-Co-Kln, and 15%-Co-HNKln demonstrated the best FTS performance. The reason that 15%-Co-HNKln exhibited the highest CO conversion rate was that it had the largest specific surface area, the most dispersed Co particles with smallest particle size, as well as the richest new active sites. Besides, as concluded in the CO-TPD analysis above, the 15%-Co-HNKln went through the most efficient acid-etching process and, thus, the surface acidity of this sample was the greatest in the samples. Because significant surface acidity was beneficial to the generation of hydrocarbons with longer chains (Wang and Hu, 2019), the 15%-Co-HNKln showed the greatest C_5–C_{12} hydrocarbon selectivity.

Conclusions

In the present study, delaminated and pit-rich nano-kaolinite was obtained via the intercalation-etching strategy, and FTS catalyst was prepared after loading Co particles on the nano-kaolinites (15%-Co-HNKln). Compared with other FTS catalysts, the supports for which were raw kaolinite or directly acid-treated kaolinite, the 15%-Co-HNKln catalyst showed several advantages such as the largest specific surface area, the most dispersed Co particles with smallest particle size, the richest new active sites, and the greatest surface acidity. Because of the advantages mentioned above, the 15%-Co-HNKln showed the best FTS performance among the three catalysts, with the highest CO conversion rate of 53.47% and the highest C_5–C_{12} hydrocarbons (gasoline) selectivity of 51.49%. Compared with that of raw

Table 4 Catalytic performance of 15%-Co-Kln,15%-Co-HKln, and 15%-Co-HNKln catalysts

Catalyst	CO Conv.[a] (%)	CH_4 Selec.[b] (%)	C_2-C_4 Selec. (%)	C_5-C_{12} Selec. (%)	C_{13}-C_{19} Selec. (%)	Oxides Selec. (%)
15%-Co-Kln	32.9	28.3	25.4	37.4	1.7	7.2
15%-Co-HKln	43.2	25.9	17.9	45.8	5.0	5.4
15%-Co-HNKln	53.5	22.3	17.0	51.5	4.8	4.4

[a]"Conv." represents "Conversion"

[b]"Selec." represents "Selectivity"

https://doi.org/10.1007/s42860-023-00249-1 Published online by Cambridge University Press

kaolinite-supported FTS catalyst, the CO conversion rate and C_5–C_{12} hydrocarbons selectivity of 15%-Co-HNKln showed increases of 20 and 15%, respectively. Clearly, the kaolinite could be modified efficiently by the intercalation-etching strategy and, therefore, the FTS performance of kaolinite-supported catalyst could be improved significantly. This study provides new guidance to the modification and catalytic application of kaolinite.

Acknowledgements The authors acknowledge funding as outlined below.

Authors' Contributions Hongxiao Qu: Writing—original draft. Tong Liu: Formal analysis. Ruijue Hu: Writing—review and editing. Hao Qu: Formal analysis. Yichi Zhang: Formal analysis. Hui Yang: Formal analysis. Haiquan Su: Funding acquisition, Data curation, Writing—review and editing. Yue Su: Conceptualization, Formal analysis, Writing—review and editing.

Funding This work was supported financially by the Major Projects of Inner Mongolia Natural Science Foundation (2019ZD01), the Application Technology Research and Development Funds of Inner Mongolia (2019GG278) and the Prairie Excellence Innovation and Entrepreneurial Team of Inner Mongolia (No.12000–12102413).

Data Availability All data generated or analysed during this study are included in this published article.

Code Availability Not applicable.

Declarations

Competing Interests On behalf of all authors, the corresponding author states that there are no conflicts of interest.

References

Abdullahi, T., & Othman, M. H. D. (2017). A review on sustainable synthesis of zeolite from kaolinite resources via hydrothermal process. *Advanced Powder Technology, 28*(8), 1827–1840.

Abukhadra, M. R., & Luqman, M. (2021). Enhancing the removal of organic and inorganic selenium ions using an exfoliated kaolinite/cellulose fibres nanocomposite. *Carbohydrate Polymers, 252*, 117163.

Adams, J. (1978). Differential scanning calorimetric study of the kaolinite: N-methylformamide intercalate. *Clays and Clay Minerals, 26*, 169–172.

Akbarzadeh, O., & Johan, M. R. (2018). Effects of cobalt loading, particle size, and calcination condition on Co/CNT catalyst performance in Fischer-Tropsch reactions. *Symmetry, 11*(1), 7.

Cai, Y. F., & Guo, Y. (2022). Surface pits stabilized Au catalyst for low-temperature CO oxidation. *Rare Metals, 41*(9), 3060–3068.

Chen, Y. H., & Lu, D. L. (2014). Amine modification on kaolinites to enhance CO_2 adsorption. *Journal of Colloid and Interface Science, 436*, 47–51.

Fischer, F., & Tropsch, H. (1926). The synthesis of petroleum at atmospheric pressures from gasification products of coal. *Brennstoff-Chemie, 7*, 97–104.

Gao, W., & Asuha, S. (2016). Direct acid activation of kaolinite and its effects on the adsorption of methylene blue. *Applied Clay Science, 126*, 98–106.

Gruner, J. W. (1932). The crystal structure of kaolinite. *Zeitschrift für Kristallographie-Crystalline Materials, 83*(1–6), 75–88.

Hai, Y., & Asuha, S. (2015). Modification of acid-activated kaolinite with TiO_2 and its use for the removal of azo dyes. *Applied Clay Science, 114*, 558–567.

Hendricks, S. B. (1936). Concerning the crystal structure of kaolinite, Al_2O_3. $2SiO_2$. $2H_2O$, and the composition of anauxite. *Zeitschrift für Kristallographie-Crystalline Materials, 95*(1–6), 247–252.

Horváth, E., & Cseh, T. (2003). Thermal treatment of mechanochemically activated kaolinite. *Thermochimica Acta, 404*(1–2), 227–234.

Hu, P., & Yang, H. (2013). Insight into the physicochemical aspects of kaolins with different morphologies. *Applied Clay Science, 74*, 58–65.

Irandoust, A., & Haghtalab, A. (2017). A hybrid reduction–impregnation method in preparation of Co–Ru/γ-Al_2O_3 catalyst for Fischer-Tropsch synthesis. *Catalysis Letters, 147*, 2967–2981.

Kelleher, B., & O'Dwyer, T. (2002a). Intercalation of benzamide into expanded kaolinite under ambient environmental conditions. *Clays and Clay Minerals, 50*(3), 331–335.

Kelleher, B., & O'Dwyer, T. (2002b). The effect of kaolinite intercalation on the structural arrangements of N-methylformamide and 1-methyl-2-pyrrolidone. *Journal of Colloid and Interface Science, 255*(2), 219–224.

Komori, Y., & Kuroda, K. (1998). A kaolinite-NMF-methanol intercalation compound as a versatile intermediate for further intercalation reaction of kaolinite. *Journal of Materials Research, 13*(4), 930–934.

Letaief, S., & Detellier, C. (2011). Single kaolinite nanometer layers prepared by an in situ polymerization–exfoliation process in the presence of ionic liquids. *Langmuir, 27*(24), 15248–15254.

Li, C., & Dionysiou, D. D. (2018). Acetic acid functionalized TiO_2/kaolinite composite photocatalysts with enhanced photocatalytic performance through regulating interfacial charge transfer. *Journal of Catalysis, 367*, 126–138.

Li, X., & Komarneni, S. (2017). Methoxy-grafted kaolinite preparation by intercalation of methanol: Mechanism of its structural variability. *Applied Clay Science, 137*, 241–248.

Li, C., & Sun, Z. (2020). Tuning and controlling photocatalytic performance of TiO_2/kaolinite composite towards ciprofloxacin: Role of 0D/2D structural assembly. *Advanced Powder Technology, 31*(3), 1241–1252.

Lim, Y. D., & Aditya, S. (2018). Enhanced field emission properties of carbon nanotube bundles confined in SiO_2 pits. *Nanotechnology, 29*(7), 075205.

Orzechowski, K., & Głowinski, J. (2006). Dielectric properties of intercalated kaolinite. *Journal of Physics and Chemistry of Solids, 67*(5–6), 915–919.

Panda, A. K., & Singh, R. K. (2010). Effect of sulphuric acid treatment on the physico-chemical characteristics of kaolin clay. *Colloids and Surfaces A: Physicochemical and Engineering Aspects, 363*(1–3), 98–104.

Prieto, G., & De Jongh, P. E. (2014). Quantitative relationship between support porosity and the stability of pore-confined metal nanoparticles studied on $CuZnO/SiO_2$ methanol synthesis catalysts. *ACS Nano, 8*(3), 2522–2531.

Qu, H., & Yang, H. (2023). Sandwich-structured nickel/kaolinite catalyst with boosted stability for dry reforming of methane with carbon dioxide. *Chemical Engineering Journal*, *453*, 139694.

Scherrer, P. (1918). Bestimmung der Grösse und der inneren Struktur von Kolloidteilchen mittels Röntgenstrahlen. *Nachrichten Von Der Gesellschaft Der Wissenschaften Zu Göttingen, Mathematisch-Physikalische Klasse, 1918*, 98–100.

Sugahara, Y., & Kato, C. (1990). Preparation of a kaolinite-polyacrylamide intercalation compound. *Clays and Clay Minerals, 38*, 137–143.

Tian, L., & Ibrahim, K. E. (2020). Insight into the loading and release properties of an exfoliated kaolinite/cellulose fiber (EXK/CF) composite as a carrier for oxaliplatin drug: Cytotoxicity and release kinetics. *ACS Omega, 5*(30), 19165–19173.

Tunney, J. J., & Detellier, C. (1997). Interlamellar amino functionalization of kaolinite. *Canadian Journal of Chemistry, 75*(11), 1766–1772.

Wada, K. (1961). Lattice expansion of kaolin minerals by treatment with potassium acetate. *American Mineralogist: Journal of Earth and Planetary Materials, 46*(1–2), 78–91.

Wang, C., & Hu, Y. H. (2019). Highly selective production of C_5–C_{12} hydrocarbons over efficient Ru/heteropoly-acid catalysts. *Fuel, 244*, 395–402.

Wang, J., & Zhang, P. (2017). Layered birnessite-type MnO_2 with surface pits for enhanced catalytic formaldehyde oxidation activity. *Journal of Materials Chemistry A, 5*(12), 5719–5725.

Wiewióra, A. (1969). Potassium acetate intercalation in kaolinite and its removal; effect of material characteristics. *Proceedings of the International Clay Conference, 1*, 723–733.

Zhang, Q., & Liu, Q. (2019). Hierarchical structure kaolinite nanospheres with remarkably enhanced adsorption properties for methylene blue. *Nanoscale Research Letters, 14*(1), 1–9.

Zhu, X., & Yan, C. (2016). Defects in structure as the sources of the surface charges of kaolinite. *Applied Clay Science, 124*, 127–136.

Zuo, X., & Yang, H. (2018). Intercalation and exfoliation of kaolinite with sodium dodecyl sulfate. *Minerals, 8*(3), 112.

https://doi.org/10.1007/s42860-023-00249-1 Published online by Cambridge University Press